Study of Self-Heating and its Effects in SOT-STT-MRAM

Tomáš Hadámek[*,†,‡], Nils Petter Jørstad[†,‡], Wolfgang Goes[§], Siegfried Selberherr[‡], and Viktor Sverdlov[†,‡]
[†] Christian Doppler Laboratory for Nonvolatile Magnetoresistive Memory and Logic at the
[‡] Institute for Microelectronics, TU Wien, Gußhausstraße 27-29, A-1040 Wien, Austria
[§] Silvaco Europe Ltd., Cambridge, United Kingdom
[*] *Email: hadamek@iue.tuwien.ac.at*

***Abstract*—We fully couple magnetization, charge, spin, and temperature dynamics to study the switching of the combined spin-orbit torque (SOT) - spin-transfer torque (STT) magnetoresistive random access memory (MRAM). To account for the increased temperature, the material parameters are scaled. In comparison to the constant temperature model, our full model shows an incubation period due to the rising temperature, in agreement with experimental data. Furthermore, we demonstrate field-free switching of the SOT-STT MRAM cell and show that the incubation time can be minimized, when sufficiently high voltages are applied.**

***Keywords*—Spintronics, SOT-MRAM, Self-Heating, Temperature Scaling, Incubation Time**

I. Introduction

SOT-MRAM has recently gained a lot of attention for its superior switching speeds compared to the widely used STT-MRAM [1], [2]. Another advantage of the SOT-MRAM is related to the three-terminal design separating the read and write currents, which results in much lower voltages across the MgO layer in the magnetic tunnel junction (MTJ), therefore preventing the occurrence of dielectric breakdown [3], [4]. During the switching process, however, strong currents flow through the heavy metal underneath the MTJ, heating up the structure, and affecting the switching behavior [1]. To fully understand the switching dynamics of the SOT-MRAM, a rigorous multi-physics model must be utilized. We present a model coupling charge, magnetization, spin, and temperature dynamics in order to study self-heating effects on the combined SOT-STT field-free switching [5], [6], [7] of a perpendicular MRAM cell.

II. Methods

In our model, the magnetization dynamics is governed by the Landau-Lifschitz-Gilbert equation, augmented by the addition of spin torques $\mathbf{T}_S$.

$$\frac{\partial \mathbf{m}}{\partial t} = -\gamma\mu_0 \mathbf{m} \times \mathbf{H}_{\text{eff}} + \alpha \mathbf{m} \times \frac{\partial \mathbf{m}}{\partial t} + \frac{1}{M_{\text{S}}}\mathbf{T}_{\text{S}} \tag{1}$$

$\mathbf{m}$ stands for the normalized magnetization, t for time, γ, μ_0 and α are the gyromagnetic ratio, vacuum permeability, and the phenomenological Gilbert damping, respectively, and M_S is the saturation magnetization. The effective field $\mathbf{H}_{\text{eff}}$ includes the anisotropy field $\mathbf{H}_{\text{aniso}}$, the exchange field $\mathbf{H}_{\text{exch}}$, and the demagnetization field $\mathbf{H}_{\text{demag}}$. As we consider the field-free switching, no external field is included. We assume a uniaxial magnetic anisotropy field of the free layer (FL) along the z-axis normal to the FL plane.

$$\mathbf{H}_{\text{aniso}} = \frac{2K_{\text{a}}}{\mu_0 M_{\text{S}}}(\mathbf{z}\cdot\mathbf{m})\mathbf{z} \tag{2}$$

K_{a} is the anisotropy energy density and $\mathbf{z}$ is the unit vector in z-direction. The exchange field is proportional to the Laplacian of the normalized magnetization.

$$\mathbf{H}_{\text{exch}} = \frac{2A_{\text{exch}}}{\mu_0 M_{\text{S}}}\nabla^2\mathbf{m}, \tag{3}$$

A_{exch} is the exchange stiffness. $\mathbf{H}_{\text{demag}}$ is solved by the hybrid finite element-boundary element method [8]. To account for the temperature T, we scale the saturation magnetization M_{S}, the anisotropy energy density K_{a}, and the exchange stiffness A_{ex} [1], [9].

$$M_{\text{S}}(T) = M_{\text{S}0}\, m_{\text{S}}(T) = M_{\text{S}0}\left(1 - \left(\frac{T}{T_{\text{C}}}\right)^b\right) \tag{4}$$

$$K_{\text{a}}(T) = K_{\text{a}0}\, m_{\text{S}}\,(T)^p \tag{5}$$

$$A_{\text{ex}}(T) = A_{\text{ex}0}\, m_{\text{S}}\,(T)^q \tag{6}$$

$M_{\text{S}0}$, $K_{\text{a}0}$, and $A_{\text{ex}0}$ are the corresponding quantities extrapolated to $0\,\text{K}$, T_{C} is the Curie temperature. b, p, and q are the scaling parameters. We model the temperature with the continuous heat flow equation.

$$c_V \rho_m \frac{\partial T}{\partial t} - \kappa \Delta T = \dot{q}_V \tag{7}$$

c_V, ρ_m, and κ stand for the heat capacity, the material density and the heat conductivity, respectively. We consider resistive heating $q_V = \mathbf{J}_{\mathbf{C}}^{\mathbf{2}}/\sigma$ due to the charge current density $\mathbf{J}_{\mathbf{C}}$ in the material with the electric conductivity σ.

The spin torques are evaluated from the spin accumulation $\mathbf{S}$ obtained from solving the coupled spin and charge drift-diffusion equations [10], [11].

$$\frac{\partial \mathbf{S}}{\partial t} = 0 = -\nabla\cdot\overline{\mathbf{J}_S} - D_e\left(\frac{\mathbf{S}}{\lambda_{sf}^2} + \frac{\mathbf{S}\times\mathbf{m}}{\lambda_J^2} + \frac{\mathbf{m}\times(\mathbf{S}\times\mathbf{m})}{\lambda_\varphi^2}\right) \tag{8}$$

$$\overline{\mathbf{J_S}} = -\frac{\mu_B}{e}\beta_\sigma \mathbf{m} \otimes \left(\mathbf{J}_C - \beta_D D_e \frac{e}{\mu_B}[(\nabla \mathbf{S})^\mathbf{T}\mathbf{m}]\right) - D_e \nabla \mathbf{S} - \theta_{\mathrm{SHA}} \frac{\mu_B}{e}\varepsilon \mathbf{J_C} \quad (9)$$

D_e is the diffusion coefficient, while λ_{sf}, λ_J, and λ_φ are the spin-flip, exchange, and dephasing lengths, respectively. μ_B is the Bohr magneton, e is the elementary charge, β_σ is the charge polarization, β_D is the diffusion polarization, and θ_{SHA} is the spin Hall angle. $\otimes$ denotes the outer product, $(.)^\mathbf{T}$ denotes the matrix transpose, and ε is the Levi-Civita tensor. Equation (8) is solved for a steady state, since the spin dynamics is considered to be three orders of magnitude faster than magnetization dynamics.

The charge current density $\mathbf{J_C}$ is obtained from solving the Laplace equation for the potential V.

$$-\nabla \cdot (\sigma \nabla V) = 0 \quad (10)$$

$$\mathbf{J}_C = -\sigma \nabla V \quad (11)$$

Inside the MTJ the conductivity varies with the relative angle of the FL and RL magnetizations [11].

At external boundaries we impose zero flux boundary conditions $\overline{\mathbf{J_S}}\mathbf{n} = 0$ and $\mathbf{J_C} \cdot \mathbf{n} = 0$, where $\mathbf{n}$ is the interface normal. At the contacts the potential is fixed with Dirichlet conditions for the applied voltage, while the spin-current and accumulations are assumed to be zero [10]. The spin and charge currents are kept continuous across internal boundaries, except for the spin current across the MTJ and HM/FM interfaces. The spin-currents across the MTJ are the same as in [12]. At the HM/FM interfaces, only the longitudinal spin-currents are kept continuous, while the transverse spin-currents $\mathbf{J}_\mathbf{S}^\perp$ are described by magnetoelectronic circuit theory [13], where it is assumed to be fully absorbed at the FM side of the interface.

$$\overline{\mathbf{J}_\mathbf{S}^\perp}\mathbf{n} = \frac{2\mu_B}{e}\big[\mathrm{Re}\{G^{\uparrow\downarrow}\}\mathbf{m} \times (\mathbf{m} \times \mathbf{V_S}) + \mathrm{Im}\{G^{\uparrow\downarrow}\}\mathbf{m} \times \mathbf{V_S}\big] \quad (12)$$

$G^{\uparrow\downarrow}$ is the complex spin-mixing conductivity, and $\mathbf{V_S} = (e/\mu_B)(D_e/\sigma)\mathbf{S}$ is the spin chemical potential on the HM side of the interface. The absorption is enforced across the first layer of elements on the FM side of the interface.

The spin torques at the HM/FM interface are given by

$$\mathbf{T_S} = \frac{2\mu_B}{d_h e}[\mathrm{Re}\{G^{\uparrow\downarrow}\}\mathbf{m} \times (\mathbf{m} \times \mathbf{V_S}) + \mathrm{Im}\{G^{\uparrow\downarrow}\}\mathbf{m} \times \mathbf{V_S}], \quad (13)$$

where d_h is the thickness of the interface layer. The spin torques from any other transverse spin currents are given by:

$$\mathbf{T_S} = -D_e \frac{\mathbf{m} \times \mathbf{S}}{\lambda_J^2} - D_e \frac{\mathbf{m} \times (\mathbf{m} \times \mathbf{S})}{\lambda_\varphi^2} \quad (14)$$

The equations are solved in three-dimensional space with the finite element method, using an extended version of our open-source solver [14].

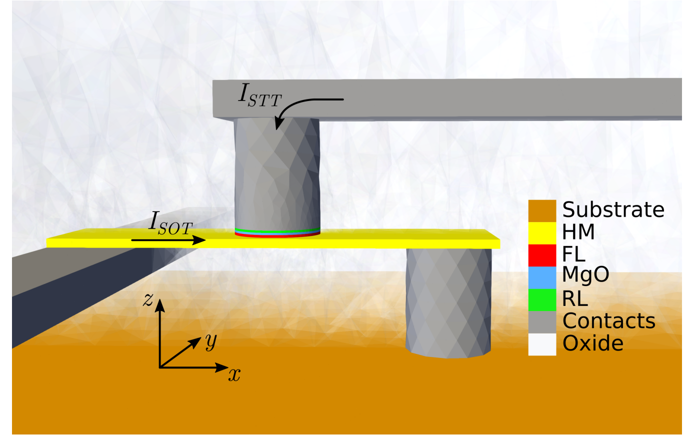

Fig. 1. The simulated structure. The separated STT and SOT current paths, and different parts of the structure are indicated.

With the described model, we simulate a realistic SOT-MRAM cell, shown in Fig. 1. A MTJ with 40 nm diameter, consisting of a 1.2 nm thick FL (red), a 1 nm thick MgO layer (blue), and a 1 nm thick reference layer (RL, green), is placed on top of a $3.7\times50\times220\,\mathrm{nm}^3$ heavy metal β-W sheet (yellow). The left side of the HM is connected to a SOT current line and the other end is contacted through a 50 nm thick via to the substrate (orange), representing an underlaying transistor and a silicon buffer. The diameter of the via is also 40 nm. On top of the MTJ, another 50 nm thick contact is placed and is connected to a STT current line (gray). The whole structure is encapsulated into $\mathrm{SiO_2}$ (white, semi-transparent). We apply Dirichlet boundary conditions (constant 300 K) on the bottom of the substrate and at the ends of the current lines, and we make sure that the boundaries are far enough away in order not to significantly affect the temperature development in our simulation window. We list the most relevant parameters in Tab. I and Tab. II. The values are mostly taken from [15]. We note that θ_{SHA}=-0.3 [16].

III. Results

The field-free switching of the SOT-STT-MRAM is performed in two steps: *i)* Both the SOT current I_{SOT} in the HM and the STT current I_{STT} through the MTJ are present. *ii)* The I_{SOT} is turned off and I_{STT} finishes the switching.

Firstly, we study the impacts of the I_{SOT} only. Fig. 2 shows a temperature profile of the simulated MRAM cell. The temperature increase is the highest around the MTJ due to heat conduction to the contacts. We remark that the heat transfer through the MgO layer is minimal due to its low thermal conductivity. In Fig. 3, a comparison between the magnetization dynamics for our full model (lower panel) and a constant-temperature model (300 K, upper panel) is shown. The constant temperature model has a sharp transition between the SOT voltages needed to flip the FL magnetization into the plane and those which fail. On the other hand, the full

TABLE I
MAGNETIZATION- AND CHARGE- AND SPIN-RELEVANT PARAMETERS.

Parameter	Value
MTJ Parameters	
Tunnel magnetoresistance ratio (TMR)	200 %
Resistance parallel	$1.4 \cdot 10^4\,\Omega$
Resistance anti-parallel	$4.2 \cdot 10^4\,\Omega$
Current spin polarization, β_σ	0.7
Diffusion spin polarization, β_D	1.0
FeCoB Parameters	
Gilbert damping, α	0.02
Gyromagnetic ratio, γ	$1.76 \cdot 10^{-11}\,\mathrm{rad} \cdot \mathrm{s}^{-1}\mathrm{T}^{-1}$
Saturation magnetization (300K), M_S	$0.81 \cdot 10^6\,\mathrm{Am}^{-1}$
Exchange stiffness (300K), A_{exch}	$2 \cdot 10^{-11}\,\mathrm{Jm}^{-1}$
Anisotropy energy density (300 K), K_a	$0.539 \cdot 10^6\,\mathrm{Jm}^{-3}$
Spin-exchange length, λ_φ	0.4 nm
Spin-dephasing length, λ_J	0.8 nm
Diffusion coefficient, D_e	$1 \cdot 10^{-3}\,\mathrm{m}^2\mathrm{s}^{-1}$
Curie temperature, T_C	750 K [17]
Scaling parameters, b, p, and q	1.7, 3, and 1.7 [1], [17]
Spin mixing conductivity, $G^{\uparrow\downarrow}$	$2 + 0.7i$

TABLE II
TEMPERATURE- AND SPIN- RELEVANT PARAMETERS.

Mat. ↓ / Par. →	σ [Ωm]	ρ_m [kg m^{-3}]	c_V [J kg^{-1}K^{-1}]	κ [W m^{-1}K^{-1}]	λ_{sf} [nm]
FeCoB	$4 \cdot 10^6$	8800	612	36	10
MgO	-	3580	877	0.4 [18]	-
β-W	$0.6 \cdot 10^6$	19300	174	134	2.4
Contacts	$7 \cdot 10^6$	8800	420	122	14
SiO_2	0	2200	730	1.4	-
Substrate	$1 \cdot 10^6$	2330	710	150	-

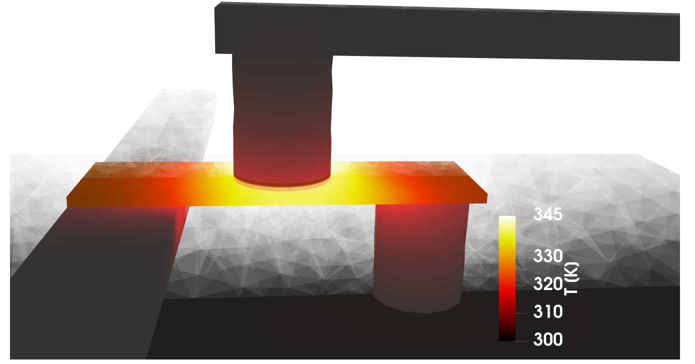

Fig. 2. Temperature of the simulated SOT-STT MRAM cell at 1 ns. The temperature is significantly increased near the MTJ.

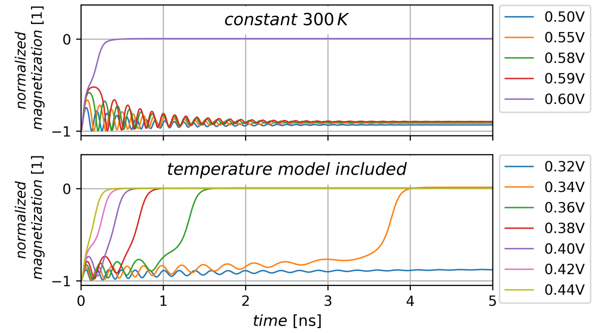

Fig. 3. FL magnetization out-of-plane to in-plane flip due to the SOT. When only a constant temperature (no thermal model included, upper plot), much higher SOT voltages are needed to bring the FL magnetization in-plane, in comparison to the full temperature model (lower plot). An incubation time similar to the one given in [1] is observed for the full temperature model.

model shows that much lower voltages are able to set the magnetization to m_z=0. Moreover, an incubation time is clearly visible, in agreement with experimental data [1]. In Fig. 4 (top panel), an average FL temperature for different SOT voltages is displayed. A sharp initial temperature increase is followed by a slower increase due to the heating of the surrounding oxide, substrate, and contacts. Due to the increased temperature, M_{S0}, A_{ex0}, and K_{a0} are reduced (lower panels), with K_{a0} contributing the most to the change of the magnetization dynamics because of the reduced energy barrier.

Secondly, we investigate the full field-free switching. Fig. 5 shows switching for different SOT voltages, while the STT voltage is kept at 1 V. The SOT voltage is turned off after 2 ns. The lower voltages show an incubation phase. For the higher voltages, the incubation phase is strongly reduced. This relatively wide time span allows for further energy and reliability optimization, and cannot be captured by the constant-temperature model. In Fig. 4, the non-trivial FL temperature behavior and parameter change for a SOT voltage of 0.3 V are shown, which fully embraces the necessity for a full temperature model inclusion.

Lastly, in Fig. 6, simulations with changing STT voltage are shown, while the SOT voltage is kept at 0.4V. For the lower STT voltages, an initial oscillation and a longer switching completion phase are observed, while on the contrary, it is diminished for the higher voltages due to the increased STTs and the increased temperature. The switching at 0 V STT and SOT voltages is only possible due to $\mathbf{H}_{\mathrm{aniso}}$ and $\mathbf{H}_{\mathrm{demag}}$ which make the magnetization relax towards the parallel orientation. We note that this switching completion is only possible for anti-parallel (AP) to parallel (P) magnetic orientation, while for P to AP a finite STT voltage is needed.

IV. CONCLUSION

We have fully coupled charge, spin, magnetization, and temperature dynamics to study combined SOT-STT-MRAM field-free switching. For lower voltages, our full model shows an incubation phase in the SOT-STT switching due to the increasing temperature and corresponding parameter change, in agreement with experimental data. The voltages required for the initialization of the switching (and hence the current densities) are significantly lower than for the constant-temperature model. The complex temperature development during the switching further underlines the necessity for the full temperature model in MRAM modeling.

ACKNOWLEDGMENTS

The financial support from the Federal Ministry of Labour and Economy, the National Foundation for Research, Technology

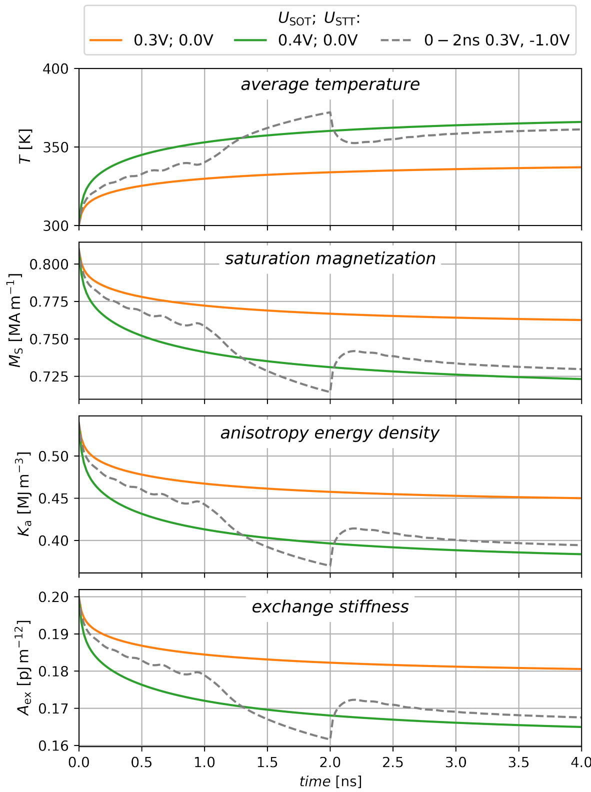

Fig. 4. Average FL temperature and parameter scaling for different SOT and STT voltages. The solid lines show simulations with only SOT voltage applied (see Fig. 3). The dashed gray lines correspond to full switching simulations with the SOT voltage applied only during the first two nanoseconds (see Fig. 5). Due to the raised temperature, the saturation magnetization, anisotropy energy density, and exchange stiffness are reduced.

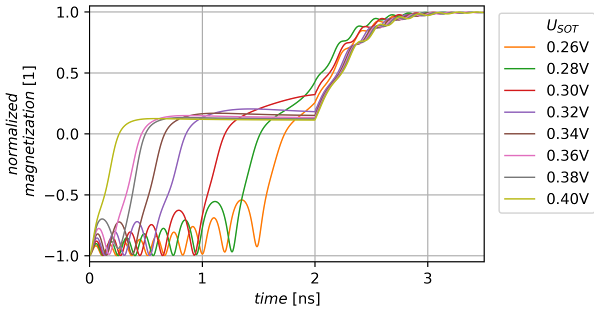

Fig. 5. Field-free STT-SOT switching for different SOT voltages. The SOT voltage is turned off after 2 ns to enable the switching to finish. The STT voltage is kept at constant 1.0 V. The lower voltages show longer incubation times. For the higher voltages, the incubation time is strongly reduced.

and Development and the Christian Doppler Research Association is gratefully acknowledged. The authors acknowledge TU Wien bibliothek for financial support through its Open Access Funding Program.

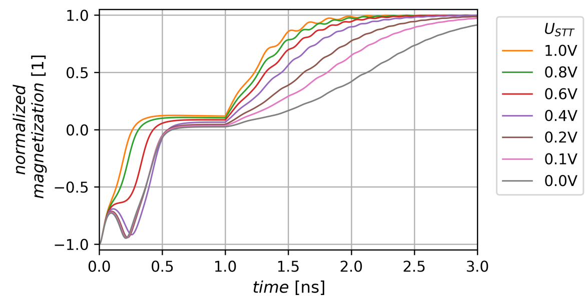

Fig. 6. Field-free STT-SOT switching for different STT voltages. The SOT voltage is turned off after 1 ns to enable the switching to finish. The SOT voltage is kept at constant 0.4 V. If the STT voltage is not high enough, an initial oscillation and a long final switching phase are observed.

References

[1] E. Grimaldi, V. Krizakova, G. Sala, F. Yasin, S. Couet *et al.*, “Single-shot dynamics of spin–orbit torque and spin transfer torque switching in three-terminal magnetic tunnel junctions,” *Nature Nanotechnology*, vol. 15, no. 2, pp. 111–117, 2020.

[2] A.D. Kent and D.C. Worledge, “A new spin on magnetic memories,” *Nature Nanotechnology*, vol. 10, no. 3, pp. 187–191, 2015.

[3] G. Panagopoulos, C. Augustine, and K. Roy, “Modeling of dielectric breakdown-induced time-dependent STT-MRAM performance degradation,” in *Device Research Conference*. IEEE, 2011, pp. 125–126.

[4] K.L. Pey, J.H. Lim, N. Raghavan, S. Mei, J.H. Kwon *et al.*, “New insights into dielectric breakdown of MgO in STT-MRAM devices,” in *Electron Devices Technology and Manufacturing Conference (EDTM)*. IEEE, 2019, pp. 264–266.

[5] A. van den Brink, S. Cosemans, S. Cornelissen, M. Manfrini, A. Vaysset *et al.*, “Spin-hall-assisted magnetic random access memory,” *Applied Physics Letters*, vol. 104, no. 1, 2014.

[6] S. Pathak, C. Youm, and J. Hong, “Impact of spin-orbit torque on spin-transfer torque switching in magnetic tunnel junctions,” *Scientific Reports*, vol. 10, no. 1, 2020.

[7] Z. Wang, W. Zhao, E. Deng, J.-O. Klein, and C. Chappert, “Perpendicular-anisotropy magnetic tunnel junction switched by spin-hall-assisted spin-transfer torque,” *Journal of Physics D: Applied Physics*, vol. 48, no. 6, p. 065001, 2015.

[8] D.R. Fredkin and T.R. Koehler, “Hybrid method for computing demagnetizing fields,” *IEEE Transactions on Magnetics*, vol. 26, no. 2, pp. 415–417, 1990.

[9] J.G. Alzate, P.K. Amiri, G. Yu, P. Upadhyaya, J.A. Katine *et al.*, “Temperature dependence of the voltage-controlled perpendicular anisotropy in nanoscale MgO|CoFeB|ta magnetic tunnel junctions,” *Applied Physics Letters*, vol. 104, no. 11, p. 112410, 2014.

[10] C. Abert, “Micromagnetics and spintronics: Models and numerical methods,” *The European Physical Journal B*, vol. 92, no. 6, 2019.

[11] S. Fiorentini, J. Ender, S. Selberherr, R.L. de Orio, W. Goes *et al.*, “Coupled spin and charge drift-diffusion approach applied to magnetic tunnel junctions,” *Solid State Electronics*, vol. 186, p. 108103, 2021.

[12] S. Fiorentini, M. Bendra, J. Ender, R.L. de Orio, W. Goes *et al.*, “Spin and charge drift-diffusion in ultra-scaled MRAM cells,” *Scientific Reports*, vol. 12, no. 1, 2022.

[13] A. Brataas, G.E.W. Bauer, and P.J. Kelly, “Non-collinear magnetoelectronics,” *Physics Reports*, vol. 427, no. 4, pp. 157–255, 2006.

[14] CDL NovoMemLog, “ViennaSpinMag,” last accessed on 29 June 2023. [Online]. Available: https://www.iue.tuwien.ac.at/viennaspinmag/

[15] S. Lepadatu, “Boris computational spintronics,” 2023, https://www.boris-spintronics.uk/, Last accessed on 14 June 2023. [Online]. Available: https://www.boris-spintronics.uk/

[16] C.-F. Pai, L. Liu, Y. Li, H.W. Tseng, D.C. Ralph, and R.A. Buhrman, “Spin transfer torque devices utilizing the giant spin hall effect of tungsten,” *Applied Physics Letters*, vol. 101, no. 12, p. 122404, 2012.

[17] K.-M. Lee, J.W. Choi, J. Sok, and B.-C. Min, “Temperature dependence of the interfacial magnetic anisotropy in w/CoFeB/MgO,” *AIP Advances*, vol. 7, no. 6, p. 065107, 2017.

[18] J. Zhang, M. Bachman, M. Czerner, and C. Heiliger, “Thermal transport and nonequilibrium temperature drop across a magnetic tunnel junction,” *Physical Review Letters*, vol. 115, no. 3, p. 037203, 2015.